

**1 Regional Base-Flow Index in Arid Landscapes Using
2 Machine Learning and Instrumented Records**

**3 Caelum Mrocze¹, Abraham Springer¹, Neha Gupta², Temuulen Sankey³,
4 Benjamin Lucas⁴**

5 ¹School of Earth and Sustainability, Northern Arizona University, Flagstaff, AZ, USA,

6 ²Department of Hydrology and Atmospheric Sciences, University of Arizona, Tucson, AZ, USA,

7 ³School of Informatics, Computing, and Cyber Systems, Northern Arizona University, Flagstaff, AZ, US,

8 ⁴Department of Mathematics and Statistics, Northern Arizona University, Flagstaff, AZ, USA,

9 **Abstract**

10 Base flow, sustained by groundwater discharge, is a vital component of river ecosystems,
 11 particularly in drylands, where water resources are limited. This study analyzes
 12 the instrumented streamflow record in Arizona to assess long-term base-flow
 13 index (BFI) trends across gauged catchments. Results indicate that approximately
 14 32% of Arizona's streamflow originates from groundwater discharge, with significant
 15 spatial variability driven by landscape and climatic factors. Base flow relationships
 16 are analyzed with coincident trends in climate variables such as precipitation, evap-
 17 otranspiration, and temperature. Spatial and climatic trends reveal variability in
 18 base-flow contributions, providing insight into groundwater-surface water interac-
 19 tions in arid and semi-arid landscapes. Building on this analysis, we applied machine
 20 learning methods to predict BFI in ungauged basins, addressing the challenges
 21 of Arizona's sparse streamgage network. Using the eXtreme Gradient Boosting
 22 (XGBoost) algorithm trained on hydroclimate and physiographic predictors, we
 23 estimated long-term BFI from 1991 to 2020. This combined approach integrates ob-
 24 servational data with predictive modeling to enhance our understanding of base-flow
 25 processes and provide a framework for water resource management in data-limited
 26 regions.

27 **Plain Language Summary**

28 Rivers in drylands, such as Arizona, depend on groundwater contributions to main-
 29 tain flow during dry periods. This portion of streamflow, called base flow, plays a
 30 critical role in supporting ecosystems and water availability in these regions. This
 31 study examines long-term patterns of base flow in Arizona using data from stream-
 32 flow monitoring stations. We found that about 32% of Arizona's river flow comes
 33 from groundwater, though this varies significantly across the state depending on
 34 local climate and landscape features. We also analyzed how base flow is influenced
 35 by changes in precipitation, evapotranspiration, and temperature, providing insights
 36 into how groundwater and surface water interact in these complex environments. To
 37 estimate base flow in basins without monitoring stations, we used machine learning
 38 techniques. By training a model on data from monitored sites and corresponding hy-
 39 droclimate data, we predicted long-term base flow for ungauged areas across Arizona.
 40 This innovative approach addresses the challenge of Arizona's sparse monitoring net-
 41 work and provides a valuable tool for understanding and managing water resources
 42 in regions with limited data.

43 **1 Introduction**

44 Dryland regions, encompassing arid, semi-arid, hyper-arid, and dry sub-humid sys-
 45 tems, account for 40% of the Earth's land surface. These regions are home to ap-
 46 proximately 2 billion people globally and constitute the largest terrestrial biome
 47 (IUCN, 2019). Despite supporting diverse ecosystems and human populations,
 48 dryland regions face mounting hydrologic challenges exacerbated by increasing ur-
 49 banization, expanding agricultural activities, and climate-induced amplification of
 50 precipitation patterns (Taylor et al., 2013). This water scarcity is intensifying due
 51 to the compounding effects of climate variability and increased groundwater extrac-
 52 tion (Taylor et al., 2013). In drylands, groundwater serves as a vital resource for
 53 sustaining ecosystems and meeting human needs (Scanlon et al., 2006; Yao et al.,
 54 2018).

55 Base flow is the sustained portion of streamflow in the absence of runoff that is de-
 56 rived from groundwater discharge (USGS, 2018). Base flow is critical to maintaining
 57 seasonal low-flow regimes, supporting aquatic ecosystems, and facilitating the trans-
 58 port of nutrients and chemicals. Base-flow contribution to streamflow can be highly
 59 variable spatially (Beck et al., 2013; Bosch et al., 2017; Singh et al., 2018), and tem-
 60 porally (Ficklin et al., 2016; Tan et al., 2020). Increasing groundwater extraction,

61 changes in land cover/land use, and changes in precipitation patterns due to climate
 62 change affect the timing and volumes of base flow (Tan et al., 2020; Taylor et al.,
 63 2013). Effective management of water quantity and quality depends on understanding
 64 seasonal and interannual base-flow patterns and long-term changes in base-flow
 65 behavior.

66 The Base-Flow Index (BFI) is the ratio of the long-term mean base-flow volume to
 67 the long-term total streamflow volume expressed as a percentage. BFI serves as a
 68 normalized measure of groundwater contribution interannually or between basins.
 69 BFI is determined by hydrograph separation and is influenced by the climate and
 70 physiographic characteristics of a catchment (Beck et al., 2013; Neff et al., 2005;
 71 Singh et al., 2018). Between catchments, base flow fluctuates according to changes
 72 in the moisture content of the vadose zone, influenced by varying levels of evapotran-
 73 spiration and aquifer storage dynamics (Bosch et al., 2017). Since BFI calculations
 74 rely on instrumented stream records, it remains unknown for ungauged catchments,
 75 which encompass most of the earth's land surface (Fekete et al., 2007). Addressing
 76 this information gap is integral to approaching a comprehensive understanding of
 77 groundwater dynamics globally.

78 Advancements in machine learning provide tools to predict hydrologic indices in un-
 79 gauged basins, addressing the limitations of sparse streamgage networks. To tackle
 80 the challenge of quantifying base flow in ungauged catchments, numerous studies
 81 have applied both regression and machine learning methods. Ahiablame et al. (2013)
 82 found that using a regression model to estimate annual base flow of ungauged catch-
 83 ments was reasonably easy and accurate. Beck et al. (2013) overcame the nonlinearity
 84 of basin characteristics and improved results of multivariate analyses by using
 85 artificial neural networks to estimate BFI globally. Singh et al. (2018) implemented
 86 a random forest algorithm to predict long-term BFI for ungauged catchments across
 87 New Zealand. These applications demonstrate the versatility and effectiveness of
 88 machine learning in capturing complex ecohydrologic dynamics and improving our
 89 understanding of groundwater contributions to streamflow.

90 This study develops a technique for estimating BFI in ungauged basins across Ari-
 91 zona and evaluates the state's long-term BFI. Regional trends in base flow and BFI
 92 at instrumented sites are also analyzed, with these trends being linked to coincident
 93 trends in precipitation, reference evapotranspiration (ET_O), and temperature over
 94 the same periods. Using a machine learning model trained on the hydrogeologic
 95 characteristics of surface water basins, we estimate the mean BFI for ungauged
 96 basins from 1991 to 2020. This approach helps address the spatial gaps in the
 97 streamgage network, which is relatively sparse across the state. The results offer
 98 novel insights into low-flow processes in both gauged and ungauged basins, enhanc-
 99 ing our understanding of climate controls on consistent flows in Arizona. This study
 100 contributes to a more comprehensive view of hydrological dynamics in the context of
 101 arid and semi-arid landscapes.

102 2 Data & Methods

103 2.1 Study Area

104 The state of Arizona, located in the southwest United States, covers a total area
 105 of 295,253 km². Arizona is divided into two primary physiographic provinces: the
 106 Colorado Plateau in the northeast, and the Basin-and-Range region in the west and
 107 south. The Central Highlands is a transition zone consisting of scattered basins sep-
 108 arated by the mountainous foothills of the Mogollon Rim. The Colorado Plateau is
 109 dominated by high-elevation desert with an average elevation of 1,936 masl (6,352
 110 ft). Mean temperatures range from -6°C (20°F) to 26°C (80°F) and it averages 580
 111 mm (23 in) of precipitation. The Basin-and-Range region has a semi-arid to arid
 112 climate with an average elevation of 490 masl (1600 ft). Average temperature ranges

113 from 15°C (60°F) to 43°C (110°F) and the region averages 200 mm (8 in) of precipi-
 114 tation annually (Arizona State Climate Office, 2024).

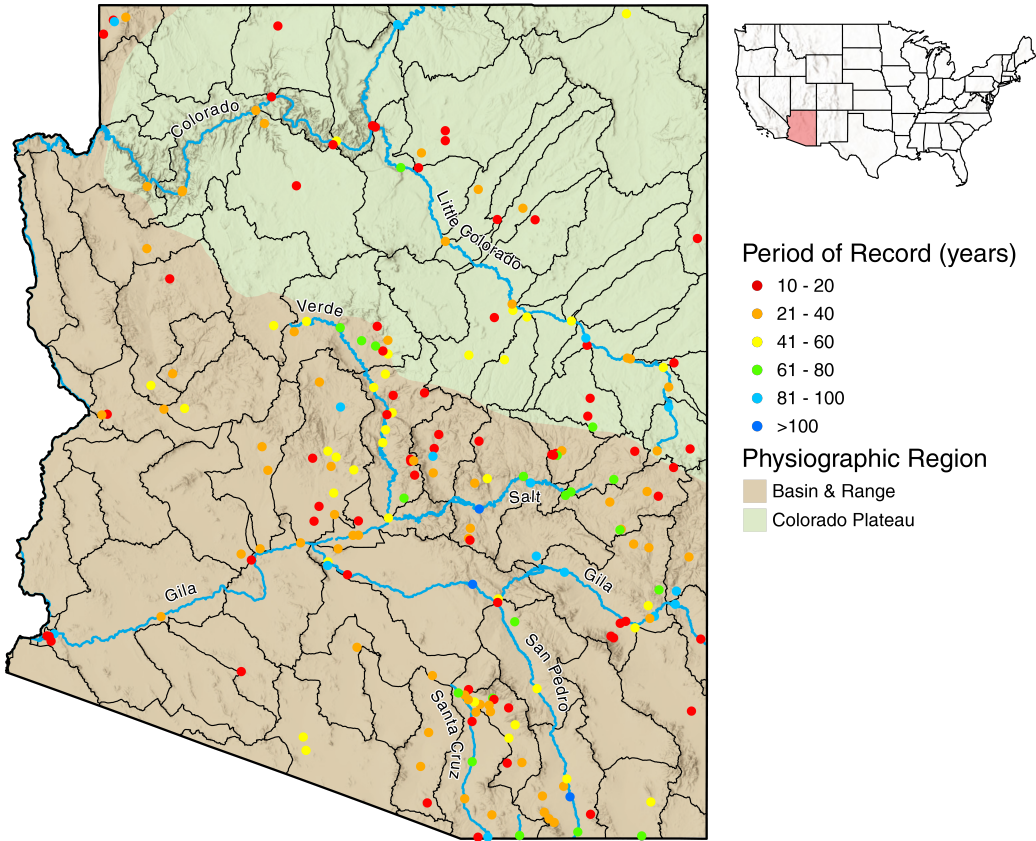


Figure 1: Map of Arizona and US Geological Survey (USGS) streamgages used in this study. 8-digit HUC subbasin boundaries and physiographic regions shown.

115 Arizona's hydrology varies seasonally and spatially between its physiographic regions.
 116 In the summer, localized and intense convective precipitation events are driven by
 117 the North American Monsoon, while in the winter, orographic precipitation comes
 118 from Pacific frontal systems (Eastoe et al., 2019). While monsoonal precipitation
 119 can account for up to 50% of annual precipitation, evaporation and dry preceding
 120 soil properties leads to most precipitation becoming runoff (Sheppard et al., 2002).
 121 As such, 94% of streams in Arizona are ephemeral or intermittent (Levick et al.,
 122 2008). Much of the hydrology of Arizona is snow-melt derived, driven by spring melt
 123 from the high-elevation Colorado Plateau winter snowpack. While winter precipi-
 124 tation provides only 30% of annual averages, it provides the majority of water for
 125 natural reservoirs (Sheppard et al., 2002).

2.2 Data

Daily observed streamflow data obtained from the United States Geological Survey (USGS) National Water Information System (NWIS) were used in this study. Streamgages were selected depending on criteria to ensure the applicability of each site. Following the findings of O'Donnell et al. (2016), which determined that 8–10 years of calibration data are necessary to account for climate variability in paired wa-
 tershed studies in the region, a minimum record length of 10 years was required. Ad-

ditionally, years with more than 30 missing days of streamflow data were excluded from the analysis. This study focuses on natural, streamflow-influencing dynamics, so streamgages affected by regulation or diversions were excluded. The regulated river streamgages were identified through annual reports on water data published by the USGS (USGS, 2010). Furthermore, streamgages along the Colorado River were omitted because they represent managed flows governed by the Colorado River Compact. After applying these selection criteria, 205 USGS streamgages with acceptable periods of record were included in the study (Figure 1). Periods of record ranged from 10 to 112 years, with a median of 28 years.

While our data selection ensures a robust record for this analysis, it also highlights gaps in spatial coverage that the machine learning model can address. Arizona has 184 active USGS streamflow stations (as of 2024) across an area of 295,253 km², whereas Indiana (a humid state in the U.S.), for example, has 189 active stations within an area of 94,326 km². This translates to a streamgage density of approximately 2.004 gages per 1,000 km² in Indiana, over three times higher than Arizona's density of 0.623 gages per 1,000 km². This stark difference underscores the relative sparsity of Arizona's streamgage network, particularly in the context of its larger geographic area and the unique hydrological challenges posed by its arid and semi-arid landscapes.

Watersheds across the United States are delineated by the USGS using a hydrologically-defined network. This system delineates the country using hierarchical hydrologic unit codes (HUCs), where each subsequent basin includes the digits of the enclosing basin. Here, 8-digit HUCs (HUC 8s) are used to divide Arizona into 84 sub-basins that are fully or partially in the state (Figure 1). These HUC 8 sub-basins are analogous to medium-sized river basins and are defined by surface water characteristics.

Annual precipitation and temperature data came from the PRISM climate group at Oregon State University at a resolution of 4 km (<https://prism.oregonstate.edu>; (Daly et al., 2008)). The PRISM dataset provides valuable insights into regional climate in ungauged regions and has been shown to perform well across the southwestern US (Buban et al., 2020). Instead of the water year, PRISM data uses a calendar-year format, which was adopted for consistency in the water balance. Although this may introduce challenges in the annual estimates due to inter-annual snow storage, the use of long-term annual averages is likely to reduce any potential errors (Reitz et al., 2017).

Annual reference evapotranspiration (ET_O) data came from TerraClimate, a 4-km grid climatological data set (Abatzoglou et al., 2018). TerraClimate uses a Penman-Monteith approach to generate a reference evapotranspiration. The ET_O values were calculated assuming a reference grass surface across the landscape with unlimited water. In the drylands of the southwestern US, ET_O typically exceeds precipitation annually (Zomer et al., 2022).

A 30-meter resolution Digital Elevation Model (DEM) of Arizona was used to derive key basin characteristics: basin area, average slope, and the proportion of each basin oriented toward north or south aspects. Various geospatial variables, such as aspect, were disaggregated then averaged to assess the areal percentage of each sub-variable within individual HUC 8 basins. By calculating these percentages, we aimed to get a more comprehensive understanding of landscape composition across space. Land cover was acquired from USGS-NLCD (National Land Cover Database), hydrologic soil group from SSURGO (Soil Survey Geographic Database), and underlying geology and karst from USGS were all similarly averaged across the basins. Aggregating variables to align with the HUC 8 boundaries allowed for more precise predictions of BFI by integrating spatial variations within each basin.

184 **2.3 Base-flow separation**

185 Directly measuring base flow and BFI presents unique challenges (Eckhardt, 2008).
 186 The technique chosen to separate base flow has been shown to affect results, and
 187 the choice of base-flow separation method is subjective since ‘true’ BFI values are
 188 not known (Beck et al., 2013). However, many methods have been developed to esti-
 189 mate these values. These methods include the use of tracers (Gonzales et al., 2009),
 190 graphical interpolation (Institute of Hydrology, 1980; Sloto et al., 1996), and digital
 191 filters (Arnold et al., 1995; Eckhardt, 2005; Lyne et al., 1979; Nathan et al., 1990).
 192 These techniques have varying levels of applicability depending on the spatial scale,
 193 time span, and the scope of the study. Comparisons of various base-flow separation
 194 techniques have been made in previous studies (e.g. Eckhardt, 2005, 2008; Nathan et
 195 al., 1990); this study does not explore the superiority of different methods.

196 Base flow was calculated using a single-parameter, recursive digital filter technique
 197 from Nathan et al. (1990). This base-flow separation technique is based on a re-
 198 cursive digital filter used in signal analysis that separates high-frequency signals
 199 (quickflow) from low-frequency signals (base flow) (Lyne et al., 1979). Eckhardt
 200 (2023) noted that recursive digital filters lack a physical basis, but as the method
 201 is easy to automate, objective, and repeatable, it is appropriate for a regional-scale
 202 study. The Lyne-Hollick filter has been used in multiple studies (Arnold et al., 2000;
 203 Bloomfield et al., 2009; Santhi et al., 2008; Singh et al., 2018), and it takes the form
 204 of

$$b = \alpha b_{k-1} + \frac{1-\alpha}{2}(Q_k + Q_{k-1}) \quad (1)$$

205 where b is base flow, α is the filter parameter, Q is the total streamflow, and k is
 206 the time step. A filter parameter α of 0.925 was used as in Nathan et al. (1990) and
 207 Fuka et al. (2014). The filter was run three times (forward, backward, forward) to
 208 attenuate the base-flow signal.

209 **2.4 Machine Learning**

210 The implementation of machine learning models to predict hydrologic indices has
 211 been successful in past studies (Rozos et al., 2021; Schmidt et al., 2020; Singh et al.,
 212 2018). In this work, we used the eXtreme Gradient Boosting (XGBoost) algorithm
 213 (Chen et al., 2016) to predict BFI at ungauged locations using catchment charac-
 214 teristics as predictors Table 1. The XGBoost algorithm is a decision tree-based
 215 ensemble algorithm, which can be adapted for either regression or classification prob-
 216 lems. This algorithm iteratively builds an ensemble of decision trees, where each
 217 tree corrects errors from previous trees to improve predictions (Chen et al., 2016).
 218 Its efficiency, scalability, and robustness have made it increasingly popular in re-
 219 cent years, with successful applications in environmental modeling tasks such as
 220 streamflow forecasting (Ni et al., 2020; Szczepanek, 2022) and land use/land cover
 221 classification (Georganos et al., 2018).

222 XGBoost operates by leveraging gradient boosting on decision tree algorithms, com-
 223 bining multiple low-variance models to produce a robust overall prediction. Gradient
 224 boosting works iteratively: the initial tree is trained on the target values, while sub-
 225 sequent trees are trained on the residual errors of the preceding tree. Each tree is
 226 assigned a weight based on its contribution to reducing error, and these weights are
 227 used to determine the influence of each tree in the final model. The ultimate predic-
 228 tion is made by aggregating the outputs of all n weighted trees in the ensemble. In
 229 this study, the trained XGBoost model is used to predict BFI in ungauged catch-
 230 ments based on geospatial and hydroclimate predictor variables (Table 1). Certain
 231 features were further subdivided according to their areal coverage within each basin
 232 (e.g. land cover was divided into 16 subdivisions). This approach allowed the model
 233 to capture finer-scale spatial variability and improve predictive accuracy.

Table 1: Basin-characteristic variables used as initial features in XGBoost model. Starred features are maintained in the final, dimensionality-reduced model.

	Variable	Source	Geoprocessing
Hydroclimate	Precipitation*	PRISM	Basin average
	Mean Temperature*	PRISM	Basin average
	Reference Evapotranspiration*	TerraClimate	Basin average
Geospatial	Elevation*	DEM	Basin average
	Area	DEM	Basin average
	Slope	DEM	Basin average
	Aspect	DEM	Percent areal coverage
	Land Cover*	NLCD	Percent areal coverage
	Hydrologic Soil Group*	SSURGO	Percent areal coverage
	Geology	USGS	Percent areal coverage
	Karst	USGS	Percent areal coverage

Our initial training dataset comprised 7,724 observations across 45 variables. To optimize the model's performance, we first conducted an exhaustive grid search combined with 5-fold cross-validation to identify the optimal hyperparameter values. The hyperparameters evaluated included the learning rate (η), minimum split loss (γ), maximum tree depth, minimum child weight, and the number of trees. While not an exhaustive list of all possible XGBoost hyperparameters, the range of values explored provided sufficient variation to ensure the selection of a high-performing model. The optimal hyperparameters were determined to be: 700 trees, a learning rate (η) of 0.05, a minimum split loss (γ) of 0.075, a maximum tree depth of 7, and a minimum child weight of 5. Using these values, the XGBoost model was trained on the dataset with 10-fold cross-validation.

K -fold cross-validation provides an unbiased estimate of a model's accuracy on unseen data, while also insuring against overfitting or underfitting. In this approach, the data are randomly divided into k folds of equal size. The model is trained on $k - 1$ folds and tested on the remaining fold, referred to as the validation set. This process is repeated k times, with each fold serving as the validation set exactly once. Each iteration trains an independent model with the same hyperparameters but using a different subset of training data. By averaging the model performance across all k folds, we achieve a robust and reliable estimate of predictive accuracy. Root mean squared error (RMSE) was used as the performance metric for both model optimization and evaluation. RMSE provided a consistent and interpretable measure of the model's accuracy throughout the training and validation process.

2.4.1 Feature Selection

Machine learning models are prone to overfitting, especially when provided with a large set of predictive features (Ying, 2019). Overfitting can degrade model performance on unseen data and increase the demand for computational resources and memory storage (Li et al., 2017). Dimensionality reduction offers a robust solution to these challenges and generally falls into two broad categories: feature extraction and feature selection.

Feature extraction involves transforming the original dataset into a lower-dimensional feature space. However, this process generates new features that often lack the physical interpretability of the original variables. In contrast, feature selection identifies a subset of the original features, preserving their physical meaning while improving model readability and interpretability (Li et al., 2017). In this study, supervised feature selection was employed to reduce the number of predictors, which enhanced learning performance, reduced computational costs, and mitigated overfitting.

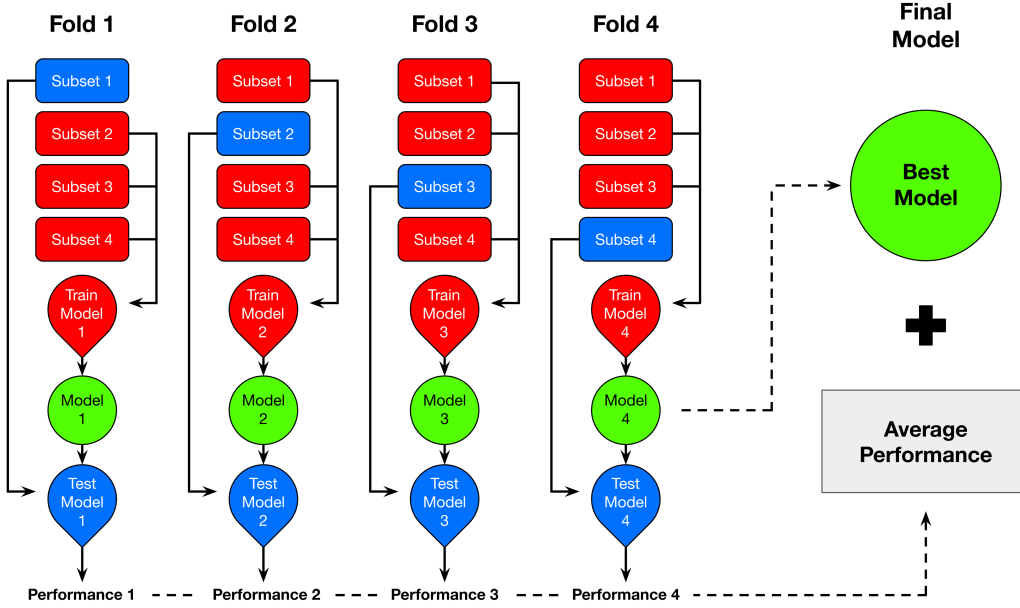


Figure 2: Schematic of k -fold cross validation. The dataset is randomly divided into k stratified folds. Each fold serves as the validation set once, while the remaining folds are combined to create a training set for model development. Performance metrics for the test set are calculated and recorded, and this process is repeated for all k folds.

To begin, an initial model was trained using the full feature set of 45 predictors (Table 1). A feature selection method based on feature importance was then applied to identify and remove less relevant and noisy features. Feature importance scores quantify the contribution of individual features—either positively or negatively—to the model’s predictions (Murdoch et al., 2019). In this analysis, SHAP (SHapley Additive exPlanations) values were used to compute feature importance scores (Lundberg & Lee, 2017).

SHAP values is a method to explain the prediction of an individual instance by calculating the contribution of each feature to that prediction. The method is based on coalition game theory and is discussed further in Lundberg & Lee (2017). Here, SHAP values are used for global interpretation of feature importance and feature effects on the model. Global feature importance is produced by the absolute Shapley values of each feature across the dataset, providing a list of features in order of most to least important. Feature effects provide an indication of the relationship between the value of a predicting feature and its impact on the prediction.

The ten most important features Figure 4 were selected based on their SHAP values and used to train a subsequent model Table 1. This refined model demonstrated improved performance and reduced computational time compared to the initial model. The final model, trained on this optimized feature subset, was ultimately used for the analysis presented here.

2.5 Statistical Analyses

Statistical analyses were conducted on annual BFI and base-flow values from instrumented streamgages to identify temporal trends using the Mann-Kendall nonparametric trend test (Kendall, 1970; Mann, 1945). This test detects monotonic trends in datasets that are non-parametric and assumes the absence of autocorrelation

295 among observations. This test is widely used in studies of this nature (Ayers et al.,
 296 2019; Ficklin et al., 2016; Woodhouse et al., 2022).

297 To check for autocorrelation, we applied the Durbin-Watson test, which revealed
 298 significant autocorrelation at four streamgages on an annual basis. Of these, only
 299 one streamgage (09486500 - Santa Cruz River at Cortaro, AZ) showed a significant
 300 trend in BFI. This streamgage was excluded from the trend analysis, as autocorrela-
 301 tion could inflate the variance of the Mann-Kendall statistic, potentially leading to
 302 biased trend estimates (Hamed & Rao, 1998). Trends with a $\rho \leq 0.05$ are considered
 303 significant.

304 3 Results

305 3.1 BFI of Ungauged Catchments

306 3.1.1 Model Validation

307 Predicted values of BFI are plotted against observed values for the entire period
 308 of record of the instrumented dataset in Figure 3 . The agreement between “out-
 309 of-bag” predictions (blind cross-validation, treating each site as ungauged) and
 310 observed values is acceptable ($R^2 = 0.764$) indicating that the model performs well
 311 across the full dataset. The overall RMSE is 0.129 and the overall percent bias
 312 (pbias) is -5.6%. Model performance metrics across various classifications are sum-
 313 marized in Table 2. These performance metrics demonstrate that the regional model
 314 performs consistently well across different spatial and climatic classifications. How-
 315 ever, the negative pbias values across all classifications, along with the overall pbias,
 316 indicate a systematic underprediction of BFI by the model. Categories with rela-
 317 tively lower R^2 and Nash-Sutcliffe Efficiency (NSE) values also exhibit higher biases,
 318 reflecting weaker model performance in those specific contexts.

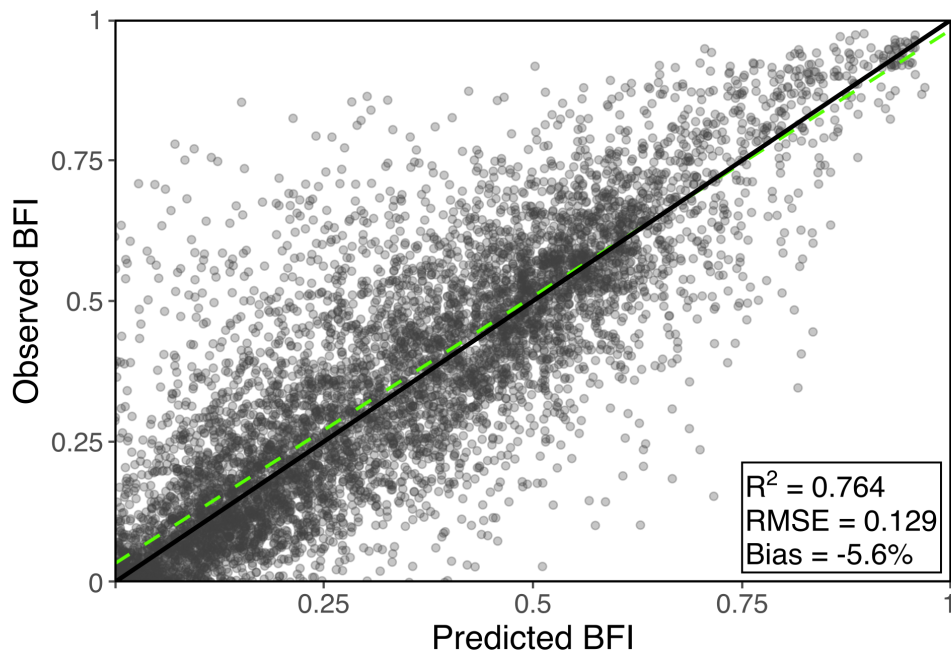


Figure 3: Linear relationship between observed BFI and predicted BFI. The solid line is the 1:1 line, the dashed, green line is regressed to the data.

Table 2: Performance of model predictions for BFI for all sites split by various classifications. n is number of observations, R^2 is the coefficient of determination of a linear regression, MSE is mean-squared-error, RMSE is root-mean-squared-error, MAE is mean-absolute-error, NSE is Nash-Sutcliffe efficiency, and pbias is percent bias.

Classification		Group	n	R2	MSE	RMSE	MAE	NSE	pbias
Climate	3039		0.633	0.016	0.126	0.074	0.619	-13.7	
- Monsoon									
Dominated									
Climate	4685		0.733	0.015	0.121	0.087	0.725	-3.5	
-									
Snowmelt									
Dominated									
PhysRegion6147			0.733	0.016	0.127	0.084	0.724	-6.3	
-									
Basin&Range									
PhysRegion1577			0.846	0.011	0.104	0.073	0.843	-3.8	
- CO									
Plateau									
Climate	1506		0.693	0.014	0.117	0.077	0.685	-8.2	
- Warm-Wet									
Climate	2351		0.693	0.022	0.147	0.092	0.675	-11.9	
- Warm-Dry									
Climate	2350		0.738	0.011	0.106	0.078	0.736	-1.7	
- Cool-Wet									
Climate	1517		0.831	0.012	0.111	0.078	0.827	-4.3	
- Cool-Dry									
Slope - High	3795		0.776	0.012	0.111	0.079	0.771	-3.3	
Slope - Low	3929		0.724	0.018	0.133	0.085	0.713	-9.1	

3.1.2 Predictor Importance

The predictors used to estimate BFI at ungauged sites were evaluated for their importance in the final XGBoost model, as illustrated in Figure 4. The most influential feature for predicting long-term BFI is basin elevation. While elevation itself does not directly affect base-flow characteristics, it has consistently been identified as a key predictor in previous BFI studies (Beck et al., 2013; Singh et al., 2018). The importance of elevation aligns with findings from Beck et al. (2013), highlighting its role as a proxy for climate variables such as temperature, precipitation, and snowpack duration. Seasonal snowpack duration, in particular, has been shown to strongly correlate with springflow and groundwater recharge in this region (Donovan et al., 2022). This relationship is further supported by hydroclimate features where higher temperatures tend to negatively influence BFI, while precipitation exhibits a mixed influence. In some cases, higher precipitation values correlate with lower BFI,

332 likely due to a larger proportion of precipitation contributing to runoff rather than
 333 infiltration and groundwater recharge.

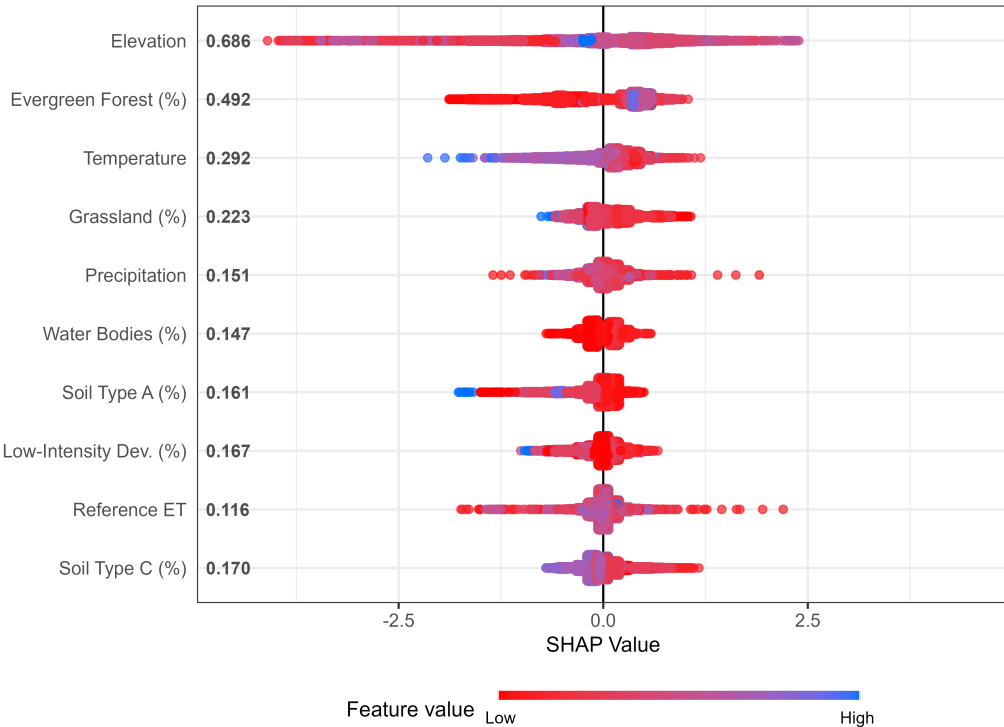


Figure 4: SHAP value plot of features used in final model. Land cover features are indicated by the percentage of cover by each land cover type and soil types are defined by hydrologic soil group.

334 Land cover and land use predictors also play a significant role in BFI estimation.
 335 Analysis of SHAP values indicates that a higher percentage of evergreen forest
 336 positively influences BFI predictions, while higher proportions of shrubland and de-
 337 veloped land exert a negative influence. Similarly, hydrologic soil types show distinct
 338 trends in their impact on BFI. Soil Type C, characterized by moderately high runoff
 339 potential (20-40% clay), tends to negatively influence BFI. In contrast, Soil Type
 340 A, which has low runoff potential and facilitates rapid water infiltration, exhibits
 341 a mixed influence (USDA, 2009). The mixed effects of Soil Type A are likely due
 342 to SHAP values capturing interactions between features rather than direct rela-
 343 tionships. For example, regions dominated by Soil Type A may also have steep slopes
 344 or sparse vegetation. Additionally, the relationship between Soil Type A and BFI
 345 is likely non-linear and influenced by the complex dynamics of regional base-flow
 346 processes.

3.1.3 Predicted Long-term BFI

The regionalized (HUC-8) long-term BFI (1991–2020) is shown in Figure 5. Basins with high BFIs, such as those along the Grand Canyon in the northwestern part of the study area, indicate greater surface water and groundwater interaction. Elevated BFI values are also observed along portions of the Mogollon Rim, a heavily forested region with high precipitation that marks the transition between physiographic regions. Additionally, headwater regions of perennial rivers tend to exhibit higher BFI values. In contrast, low BFI values are found in areas like the Defiance Plateau in

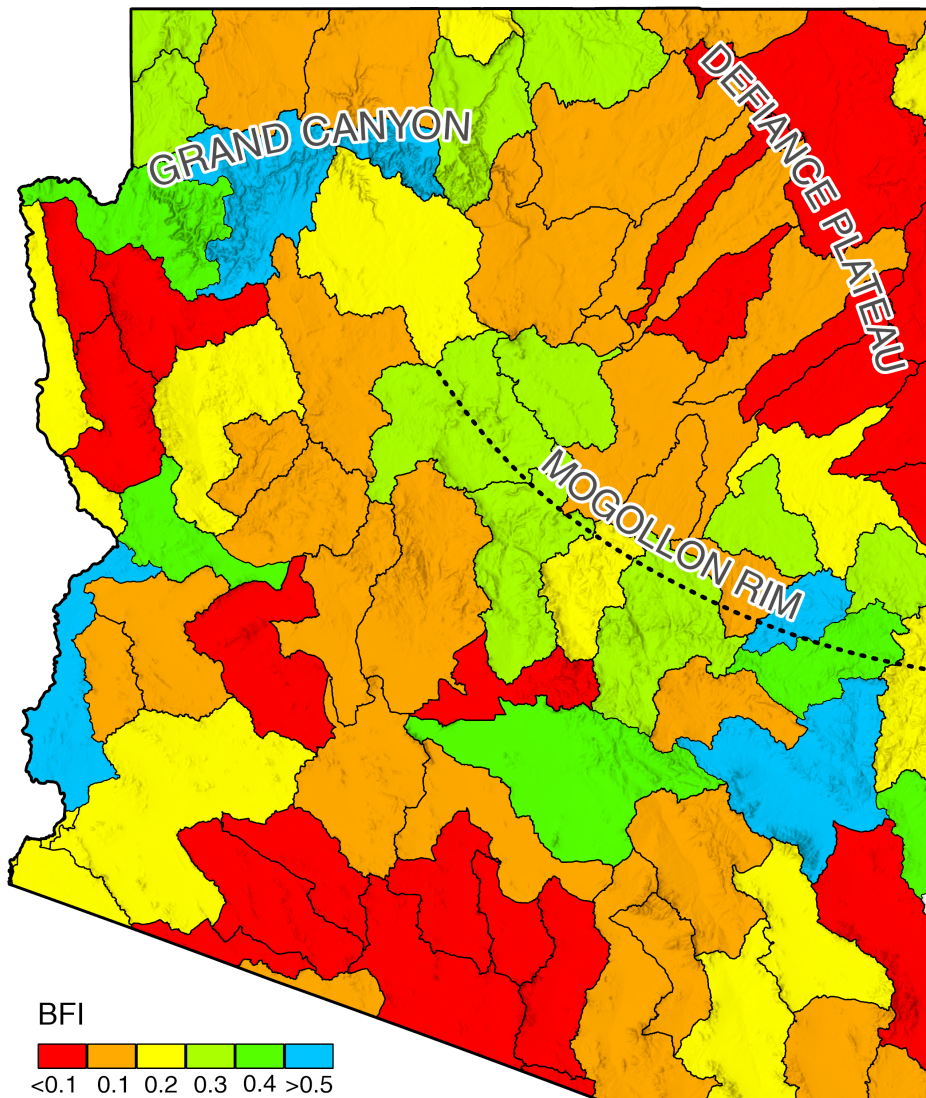


Figure 5: Predicted long-term BFI values for 8-digit HUC (1991-2020)

355 northeastern Arizona and the arid southern regions of the state. While BFI values
 356 and their spatial patterns may align with certain terrain features or climatic pat-
 357 terns, it is important to recognize that BFI is driven by complex interactions among
 358 multiple factors Figure 4.

359 **3.2 BFI of Gauged Catchments**

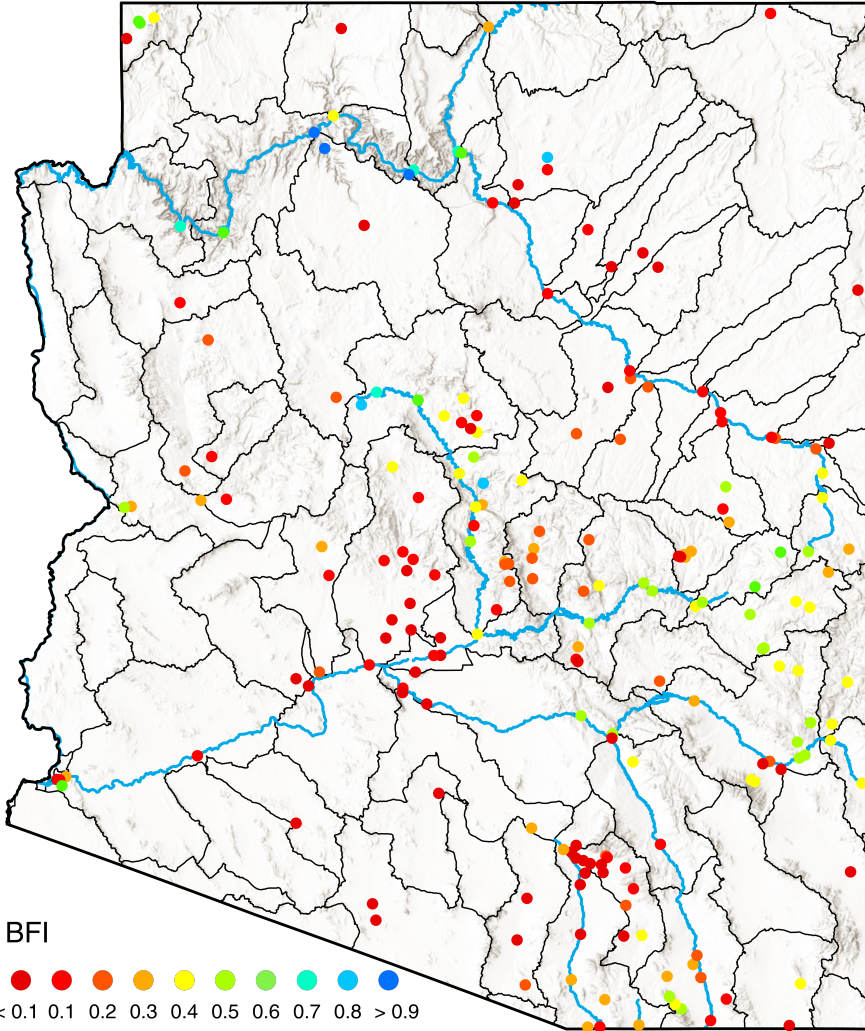


Figure 6: Long-term BFI for the period of record from instrumented stream flow data.

360 The long-term BFI for the 205 gauged reaches across Arizona is illustrated in Fig-
 361 ure 6 . The long-term mean BFI is 0.32, indicating that ~32% of long-term stream-
 362 flow in Arizona likely originates from groundwater discharge and other delayed
 363 sources. The highest BFI values (>0.9) are found along the Grand Canyon in north-
 364 western Arizona. The highly karstic geology of this region facilitates the rapid move-
 365 ment of subsurface flow to surface water and spring outlets (Chambless et al., 2023).
 366 Relatively high BFI values (>0.8) are found at the spring-fed headwaters of the
 367 Verde River (Del Rio Spring) and the spring-fed headwaters of Fossil Creek. These
 368 results are consistent with interpolated BFI values reported by Wolock (2003).

The stream reaches of the Little Colorado River Basin (northeastern Arizona) indicate consistently low BFI values (< 0.2). This is likely due to low-yielding perched aquifers underlying the Defiance Plateau in northeastern Arizona, which are hydrologically connected to surface streams, while the high-yield, confined regional aquifer is much deeper (Blanchard, 2002). A notable tendency emerges along most major rivers in the study area: upstream reaches tend to exhibit higher BFI values, while downstream reaches display lower values. This pattern is presumed to result from greater groundwater-surface water interactions at stream headwaters, influenced by spring outlets, and the dilution of base flow as water moves downstream. This trend is particularly evident along the Gila River, Verde River, and Little Colorado River in Arizona.

3.2.1 Trends in Base Flow & BFI

Trends in BFI over the period of record for each streamgage in this analysis are illustrated in Figure 7 and Table 3. Base flow and BFI trends were analyzed across all instrumented sites over their respective periods of record using the Mann-Kendall test. Statistically significant trends were observed in both metrics, with a 72.20% coincidence rate between significant base flow and BFI trends, indicating a strong dependence of BFI on base-flow dynamics.

Figure 7 illustrates the spatial variation in BFI trends across the study area. Statistically significant decreasing trends are observed at 16.1% of sites, while increasing trends are found at 8.8% of sites, with no clear regional patterns for either. In the Basin and Range physiographic region, 9% of sites show increasing trends, while 16.7% exhibit decreasing trends. In the Colorado Plateau region, increasing trends occur at 6.1% of sites, and decreasing trends are observed at 14.3% of sites.

3.2.2 Classification Trends

Classifications presented in Table 3 were determined based on precipitation regime, physiographic region, climate, and slope. The dominant precipitation regime (monsoon vs. snowmelt) was identified by analyzing streamflow hydrographs for each station, focusing on peak flow periods during the monsoon season (July–September) and the snowmelt season (March–June). Physiographic region was assigned based on which region the streamgage is located. Climate classifications were defined as warm (above the long-term median temperature of Arizona), cool (below the long-term median temperature), wet (above the long-term median precipitation), and dry (below the long-term median precipitation). Slope was categorized as high (above the median slope) and low (below the median slope).

Statistically significant decreasing trends in BFI were more common than increasing trends across all site classifications (Table 3). While decreasing trends dominate, both increasing and decreasing trends are observed within each classification. Monsoon-dominated regions exhibit a higher proportion of significant negative trends (24.1%) compared to snowmelt-dominated regions (10.2%), suggesting that monsoon-dominated systems are more consistently correlated with declining base flow. Among climate classifications, warm-dry climates have the highest proportion of negative trends (20.0%), followed by warm-wet climates (19.4%), indicating that regions with higher temperatures are more prone to base flow declines. Low-slope regions show a greater prevalence of negative trends (20.4%) compared to high-slope regions (11.8%). This suggests that flatter areas may be more susceptible to base-flow reductions, potentially due to differences in hydrologic connectivity and recharge dynamics.

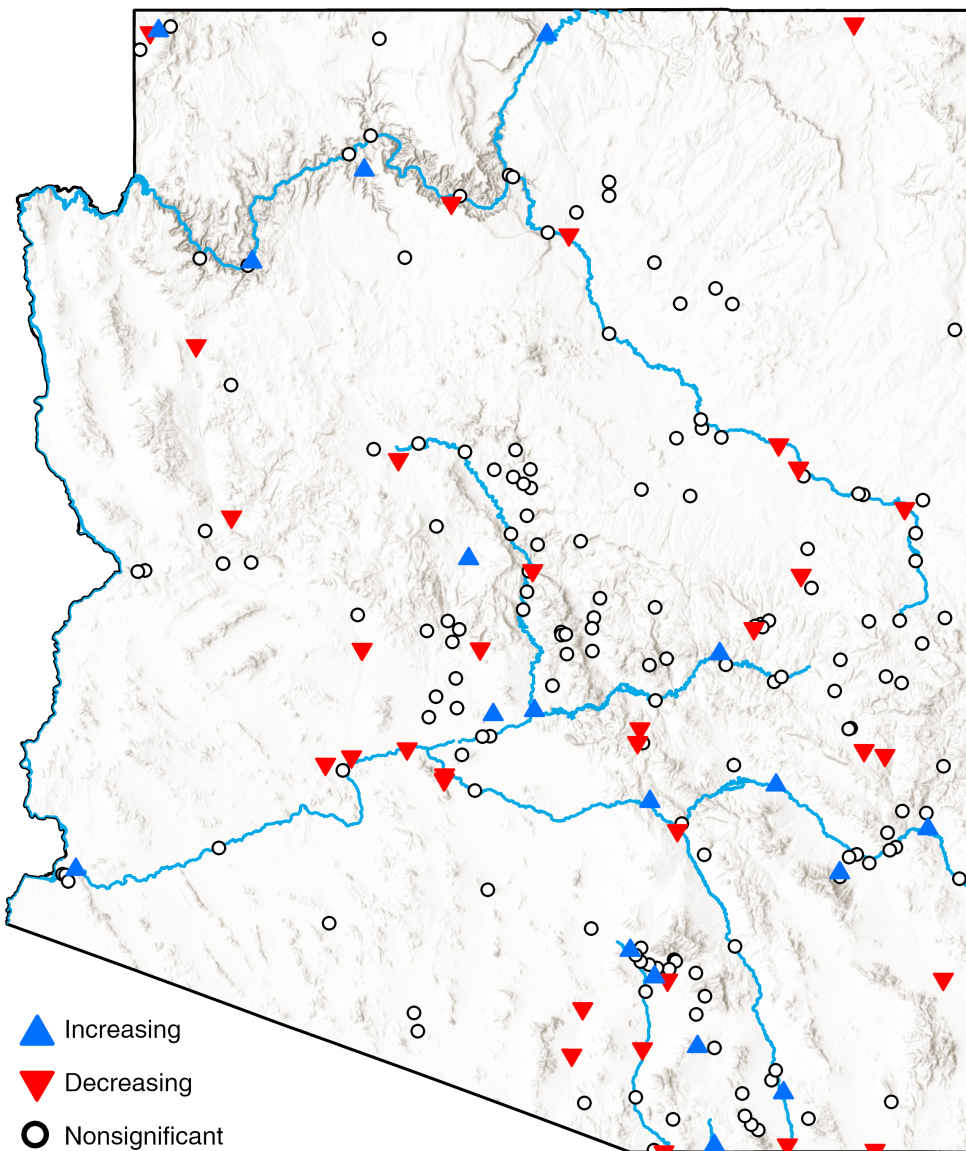


Figure 7: Trends in BFI over full period of record for instrumented sites used in this study. Red upward (blue downward) arrows indicate an increasing (decreasing) trend at a significance level of 5%. White circles represent sites with no statistically significant trends.

Table 3: Comparison of trends for BFI for all sites split by various classifications. Only sites with a significant ($\rho \leq 0.05$) trend are included here as established by a Mann-Kendall test for monotonic trends across the full period of record. n is the number of sites, n_pos (n_neg) is the number of sites with positive (negative) trends, perc_pos (perc_neg) is the percentage of n with a positive (negative) trend.

Classification					
Group	n	n_pos	n_neg	perc_pos	perc_neg
Precipitation	87	8	21	0.092	0.241
- Monsoon					
Dominated					
Precipitation	118	9	12	0.076	0.102
- Snowmelt					
Dominated					
Physiographic	156	14	26	0.090	0.167
Region -					
Basin and					
Range					
Physiographic	49	3	7	0.061	0.143
Region -					
Colorado					
Plateau					
Climate -	31	2	6	0.065	0.194
Warm-Wet					
Climate -	55	6	11	0.109	0.200
Warm-Dry					
Climate -	74	4	9	0.054	0.122
Cool-Wet					
Climate -	45	5	7	0.111	0.156
Cool-Dry					
Slope - High	102	10	12	0.098	0.118
Slope - Low	103	7	21	0.068	0.204

3.2.3 Coincident Climate Trends

Given the variations in the period of record across the instrumented network (see Figure S2), we analyzed trends in base flow and BFI in relation to coincident trends in climate variables. Trends are classified as coincident when the direction of the climate variable trend (positive or negative) aligns with the trend observed in base flow or BFI (Table 4). This analysis includes both significant and non-significant trends, which is appropriate where the influence of complex, interconnected processes may not always manifest as statistically significant patterns over limited observational periods (Ficklin et al., 2016).

Table 4: Coincident trends of climate variables (ET_O , precipitation, temperature) with base flow and BFI trends.

	Climate Variable	Coincidence Percentage (%)
BFI	ET_O	44.88
	Precipitation	53.17
	Temperature	47.32
	ET_O	55.12
	Precipitation	64.88
Base Flow		

Climate Variable	Coincidence Percentage (%)
Temperature	39.02

The analysis shows that base flow and BFI trends most frequently align with precipitation trends (64.88% and 53.17%, respectively), emphasizing precipitation as the primary driver of local groundwater recharge and discharge. Coincidence with ET_O (reference evapotranspiration) trends (55.12% for base flow and 44.88% for BFI) suggests that evapotranspiration also plays a significant role, particularly in arid regions where it can reduce recharge or base flow during dry periods. In contrast, temperature trends show lower percentages of coincidence, often opposing base flow and BFI trends. Specifically, positive (negative) temperature trends are frequently associated with negative (positive) base-flow trends (60.98%) and BFI trends (52.68%). These results highlight the complex interplay between climatic variables and hydrological processes. While precipitation exerts the strongest influence on base flow and BFI, evapotranspiration and temperature add further variability in specific environmental contexts.

4 Summary & Conclusions

This study provides new insights into base-flow dynamics and groundwater contributions in Arizona's dryland rivers by combining an analysis of instrumented streamflow records with machine learning predictions for ungauged basins. The results highlight significant spatial variability in BFI, with approximately 32% of Arizona's long-term streamflow originating from groundwater discharge. Regions such as the Grand Canyon and Mogollon Rim demonstrate high BFI values due to strong groundwater-surface water interactions, while areas like the Little Colorado River Basin exhibit low BFI values, reflecting limited groundwater recharge (Figure 5).

Using an XGBoost machine learning algorithm, we successfully predicted long-term BFI in ungauged basins, achieving strong model performance ($R^2 = 0.764$, RMSE = 0.129). The model performed well across all classifications, demonstrating its robustness in capturing base-flow dynamics across a region with substantial variability in climate, elevation, and physiographic characteristics (Table 2). Key predictors included elevation, land cover, and soil type, highlighting the importance of integrating hydroclimate and physiographic characteristics into regional hydrological models (Figure 4). These predictions address the limitations posed by Arizona's sparse streamgage network, offering a scalable approach to estimate BFI in data-limited regions.

Our analysis of BFI trends in gauged catchments revealed that precipitation is the primary driver of base-flow variability, with evapotranspiration and temperature contributing additional complexity (Table 4). These findings emphasize the critical role of climate-hydrology interactions in shaping groundwater contributions to streamflow. Inverse trends between temperature and BFI suggest that further warming could reduce groundwater contributions to streamflow. Coincident trends in precipitation and BFI further underscore the importance of understanding recharge processes, especially in arid and semi-arid landscapes, where precipitation events play key roles in replenishing groundwater.

The utility of the streamgage networks for base-flow analyses in Arizona is limited by their design and focus. There has been an increase in the number of streamgages in the region to meet regulatory imperatives, such as the Clean Water Act. Even so, many of these gages are not suited for base-flow studies because they emphasize peak flow monitoring and lack the ability to accurately measure low-flow dynamics (Maricopa County, 2020). New, non-USGS streamgages are typically installed by flood control districts (e.g. the ALERT system) and are designed to track flood flows rather than base flow. New USGS streamgages have been added over the past

475 decade to address instream flow rights and to improve the density of monitoring in
 476 the future.

477 This study demonstrates the benefits of combining observational records with ma-
 478 chine learning to improve our understanding of streamflow processes in drylands.
 479 Future work should explore the projected effects of climate change on base-flow pro-
 480 cesses and developing models for other data-poor regions. The framework presented
 481 here has broad applicability to other arid and semi-arid regions worldwide and can
 482 inform water resource management strategies aimed at addressing water scarcity and
 483 adapting to climate variability.

484 5 Open Research

485 All code and data necessary to reproduce the analyses presented in this manuscript
 486 are available at: <https://github.com/CaelumMroczeck/baseflow-AZ>.

487 6 Acknowledgements

488 The authors would like to express gratitude to the following people for helpful dis-
 489 cussion and suggestions: Cole Denver, Aidan Houlgate, Rayni Lewis, Ryan Lima,
 490 Quentin McCalla, Isaiah Mesa, Georgia Roberts. This research was supported by
 491 an Arizona Board of Regents' Grant from the Technology and Research Initiative
 492 Fund governed by A.R.S. § 15-1648. The authors acknowledge the financial support
 493 provided by this grant, which made this study possible.

494 References

- 495 Abatzoglou, J. T. et al. (2018). TerraClimate, a high-resolution global dataset of
 496 monthly climate and climatic water balance from 1958–2015. *Scientific Data*,
 497 5(1), 170191. <https://doi.org/10.1038/sdata.2017.191>
- 498 Ahiablame, L. et al. (2013). Estimation of annual baseflow at ungauged sites in
 499 Indiana USA. *Journal of Hydrology*, 476, 13–27. <https://doi.org/10.1016/j.jhydrol.2012.10.002>
- 500 Arizona State Climate Office. (2024). Climate of Arizona. Retrieved from <https://globalfutures.asu.edu/azclimate/climate/>
- 501 Arnold, J. G. et al. (1995). Automated Base Flow Separation and Recession Analy-
 502 sis Techniques. *Ground Water*, 33(6), 1010–1018. <https://doi.org/10.1111/j.1745-6584.1995.tb00046.x>
- 503 Arnold, J. G. et al. (2000). Regional estimation of base flow and groundwater
 504 recharge in the upper mississippi river basin. *Journal of Hydrology*, 227(1),
 505 21–40. [https://doi.org/10.1016/S0022-1694\(99\)00139-0](https://doi.org/10.1016/S0022-1694(99)00139-0)
- 506 Ayers, J. R., Villarini, G., Jones, C., & Schilling, K. (2019). Changes in monthly
 507 baseflow across the U.S. Midwest. *Hydrological Processes*, 33(5), 748–758.
 508 <https://doi.org/10.1002/hyp.13359>
- 509 Beck, H. E. et al. (2013). Global patterns in base flow index and recession based
 510 on streamflow observations from 3394 catchments: Global Patterns in Base
 511 Flow Characteristics. *Water Resources Research*, 49(12), 7843–7863. <https://doi.org/10.1002/2013WR013918>
- 512 Blanchard, P. J. (2002). *Assessments of aquifer sensitivity on Navajo Nation and
 513 adjacent lands and ground-water vulnerability to pesticide contamination on the
 514 Navajo Indian Irrigation Project, Arizona, New Mexico, and Utah* (No. Water-
 515 Resources Investigations Report 02-4051). USGS. <https://doi.org/10.3133/wri024051>
- 516 Bloomfield, J. P. et al. (2009). Examining geological controls on baseflow in-
 517 dex (BFI) using regression analysis: An illustration from the Thames Basin,
 518 UK. *Journal of Hydrology*, 373(1-2), 164–176. <https://doi.org/10.1016/j.jhydrol.2009.04.025>

- Bosch, D. D. et al. (2017). Temporal variations in baseflow for the Little River experimental watershed in South Georgia, USA. *Journal of Hydrology: Regional Studies*, 10, 110–121. <https://doi.org/10.1016/j.ejrh.2017.02.002>
- Buban, M. S. et al. (2020). A comparison of the u.s. Climate reference network precipitation data to the parameter-elevation regressions on independent slopes model (PRISM). *Journal of Hydrometeorology*, 21(10), 2391–2400. <https://doi.org/10.1175/JHM-D-19-0232.1>
- Chambless, H. E. et al. (2023). Deep-karst aquifer spring-flow trends in a water-limited system, grand canyon national park, USA. *Hydrogeology Journal*, 31(7), 1755–1771. <https://doi.org/10.1007/s10040-023-02702-w>
- Chen, T. et al. (2016). Xgboost: A scalable tree boosting system. In *Proceedings of the 22nd acm sigkdd international conference on knowledge discovery and data mining* (pp. 785–794).
- Daly, C. et al. (2008). Physiographically sensitive mapping of climatological temperature and precipitation across the conterminous United States. *International Journal of Climatology*, 28(15), 2031–2064. <https://doi.org/10.1002/joc.1688>
- Donovan, K. M. et al. (2022). Karst spring processes and storage implications in high elevation, semiarid southwestern united states. In M. J. Currell & B. G. Katz (Eds.), *Geophysical monograph series* (1st ed., pp. 35–50). Wiley. <https://doi.org/10.1002/9781119818625.ch4>
- Eastoe, C. J. et al. (2019). Hydrology of mountain blocks in arizona and new mexico as revealed by isotopes in groundwater and precipitation. *Geosciences*, 9(11). <https://doi.org/10.3390/geosciences9110461>
- Eckhardt, K. (2005). How to construct recursive digital filters for baseflow separation. *Hydrological Processes*, 19(2), 507–515. <https://doi.org/10.1002/hyp.5675>
- Eckhardt, K. (2008). A comparison of baseflow indices, which were calculated with seven different baseflow separation methods. *Journal of Hydrology*, 352(1-2), 168–173. <https://doi.org/10.1016/j.jhydrol.2008.01.005>
- Eckhardt, K. (2023). Technical note: How physically based is hydrograph separation by recursive digital filtering? *Hydrology and Earth System Sciences*, 27(2), 495–499. <https://doi.org/10.5194/hess-27-495-2023>
- Fekete, B. M. et al. (2007). The current status of global river discharge monitoring and potential new technologies complementing traditional discharge measurements.
- Ficklin, D. L. et al. (2016). Impacts of recent climate change on trends in baseflow and stormflow in United States watersheds. *Geophysical Research Letters*, 43(10), 5079–5088. <https://doi.org/10.1002/2016GL069121>
- Fuka, D. et al. (2014). EcoHydRology: A community modeling foundation for eco-hydrology. *R Package Version 0.4, 12*.
- Georganos, S. et al. (2018). Very high resolution object-based land use–land cover urban classification using extreme gradient boosting. *IEEE Geoscience and Remote Sensing Letters*, 15, 607–611. <https://doi.org/10.1109/LGRS.2018.2803259>
- Gonzales, A. L. et al. (2009). Comparison of different base flow separation methods in a lowland catchment. *Hydrology and Earth System Sciences*, 13(11), 2055–2068. <https://doi.org/10.5194/hess-13-2055-2009>
- Hamed, K. H., & Rao, A. (1998). A modified mann-kendall trend test for autocorrelated data. *Journal of Hydrology*, 204(1), 182–196. [https://doi.org/10.1016/S0022-1694\(97\)00125-X](https://doi.org/10.1016/S0022-1694(97)00125-X)
- Institute of Hydrology. (1980). *Low flow studies report 3 catchment characteristic estimation manual*.
- IUCN. (2019, September). Drylands and climate change. Retrieved from <https://www.iucn.org/resources/issues-brief/drylands-and-climate-change>

- 580 Kendall, M. G. (1970). *Rank correlation methods* (4th ed). London: Griffin.
- 581 Levick, L. R. et al. (2008). The ecological and hydrological significance of ephemeral
582 and intermittent streams in the arid and semi-arid American Southwest. *U.S.
583 Environmental Protection Agency and USDA/ARS Southwest Watershed Re-
584 search Center*, (EPA/600/R-08/134).
- 585 Li, J., Cheng, K., Wang, S., Morstatter, F., Trevino, R. P., Tang, J., & Liu, H.
586 (2017). Feature selection: A data perspective. *ACM Comput. Surv.*, 50(6).
587 <https://doi.org/10.1145/3136625>
- 588 Lundberg, S. M., & Lee, S.-I. (2017). A unified approach to interpreting model pre-
589 dictions, 30. Retrieved from https://proceedings.neurips.cc/paper_files/paper/2017/file/8a20a8621978632d76c43dfd28b67767-Paper.pdf
- 590 Lyne, V. et al. (1979). Institute of engineers australia national conference. In (Vol.
591 79, pp. 89–93). Barton, Australia: Institute of Engineers Australia.
- 592 Mann, H. B. (1945). Nonparametric tests against trend. *Econometrica: Journal of
593 the Econometric Society*, 245–259.
- 594 Maricopa County, F. C. D. of. (2020). *Flood Warning Program - Program Re-
595 view*. Maricopa County Flood Control District. Retrieved from https://alert.fcd.maricopa.gov/alert/FWP_report_FINAL.pdf
- 596 Murdoch, W. J., Singh, C., Kumbier, K., Abbasi-Asl, R., & Yu, B. (2019). Defini-
597 tions, methods, and applications in interpretable machine learning. *Proceedings
598 of the National Academy of Sciences*, 116(44), 22071–22080. <https://doi.org/10.1073/pnas.1900654116>
- 599 Nathan, R. J. et al. (1990). Evaluation of automated techniques for base flow and
600 recession analyses. *Water Resources Research*, 26(7), 1465–1473. <https://doi.org/10.1029/WR026i007p01465>
- 601 Neff, B. P. et al. (2005). *Base flow in the great lakes basin* (Report No. 2005-5217).
602 Reston, VA. <https://doi.org/10.3133/sir20055217>
- 603 Ni, L. et al. (2020). Streamflow forecasting using extreme gradient boosting model
604 coupled with gaussian mixture model. *Journal of Hydrology*, 586, 124901.
- 605 O'Donnell, F. C. et al. (2016). 12th Biennial Conference of Research on the Col-
606 orado Plateau. In.
- 607 Reitz, M. et al. (2017). Annual Estimates of Recharge, Quick-Flow Runoff, and
608 Evapotranspiration for the Contiguous US Using Empirical Regression Equations.
609 *JAWRA Journal of the American Water Resources Association*, 53(4), 961–983.
610 <https://doi.org/10.1111/1752-1688.12546>
- 611 Rozos, E. et al. (2021). Machine learning in assessing the performance of hydrologi-
612 cal models. *Hydrology*. <https://doi.org/10.3390/hydrology9010005>
- 613 Santhi, C. et al. (2008). Regional estimation of base flow for the conterminous
614 United States by hydrologic landscape regions. *Journal of Hydrology*, 351(1-2),
615 139–153. <https://doi.org/10.1016/j.jhydrol.2007.12.018>
- 616 Scanlon, B. R. et al. (2006). Global synthesis of groundwater recharge in semiarid
617 and arid regions. *Hydrological Processes*, 20(15), 3335–3370. <https://doi.org/10.1002/hyp.6335>
- 618 Schmidt, L. et al. (2020). Challenges in applying machine learning models for hy-
619 drological inference: A case study for flooding events across germany. *Water
620 Resources Research*, 56(5), e2019WR025924. <https://doi.org/https://doi.org/10.1029/2019WR025924>
- 621 Sheppard, P. et al. (2002). The climate of the US Southwest. *Climate Research*, 21,
622 219–238. <https://doi.org/10.3354/cr021219>
- 623 Singh, S. K. et al. (2018). Towards baseflow index characterisation at national
624 scale in New Zealand. *Journal of Hydrology*, 568, 646–657. <https://doi.org/10.1016/j.jhydrol.2018.11.025>
- 625 Sloto, R. et al. (1996). *HYSEP: A Computer Program for Streamflow Hydrograph
626 Separation and Analysis* (No. 96-4040). USGS. <https://doi.org/10.3133/wri964040>

- 635 Szczepanek, R. (2022). Daily streamflow forecasting in mountainous catchment
636 using XGBoost, LightGBM and CatBoost. *Hydrology*, 9(12), 226.
- 637 Tan, X. et al. (2020). Global Changes in Baseflow Under the Impacts of Changing
638 Climate and Vegetation. *Water Resources Research*, 56(9), e2020WR027349.
639 <https://doi.org/10.1029/2020WR027349>
- 640 Taylor, R. G. et al. (2013). Ground water and climate change. *Nature Climate
641 Change*, 3(4), 322–329. <https://doi.org/10.1038/nclimate1744>
- 642 USDA. (2009). *Part 630 hydrology national engineering handbook, chapter 7: Hydro-
643 logic soil groups*. USDA Natural Resources Conservation Service.
- 644 USGS. (2010). Water resources data for the united states water year 2007. <http://wdr.water.usgs.gov/wy2007/search.jsp>.
- 645 USGS. (2018). Water science glossary. Retrieved from <https://www.usgs.gov/special-topics/water-science-school/science/water-science-glossary>
- 646 Wolock, D. M. (2003). Estimated mean annual natural ground-water recharge in the
647 conterminous united states. <https://doi.org/10.5066/P9FSSVF3>.
- 648 Woodhouse, C. A. et al. (2022). Upper Gila, Salt, and Verde Rivers: Arid Land
649 Rivers in a Changing Climate. *Earth Interactions*, 26(1), 1–14. <https://doi.org/10.1175/EI-D-21-0014.1>
- 650 Yao, Y. et al. (2018). Role of Groundwater in the Dryland Ecohydrological Sys-
651 tem: A Case Study of the Heihe River Basin. *Journal of Geophysical Research:
Atmospheres*, 123(13), 6760–6776. <https://doi.org/10.1029/2018JD028432>
- 652 Ying, X. (2019). An overview of overfitting and its solutions. *Journal of Physics:
Conference Series*, 1168(2), 022022. <https://doi.org/10.1088/1742-6596/1168/2/022022>
- 653 Zomer, R. J. et al. (2022). Version 3 of the Global Aridity Index and Potential
654 Evapotranspiration Database. *Scientific Data*, 9(1), 409. <https://doi.org/10.1038/s41597-022-01493-1>
- 655
- 656
- 657
- 658
- 659
- 660
- 661